

Machine-learning-accelerated simulations enable heuristic-free surface reconstruction

Xiaochen Du^{1,2}, James K. Damewood^{3,2}, Jaclyn R. Lunger³, Reisel Millan³, Bilge Yildiz^{4,3}, Lin Li⁵ and Rafael Gómez-Bombarelli^{3*}

¹Department of Chemical Engineering, Massachusetts Institute of Technology, 77 Massachusetts Ave, Cambridge, MA, 02139, USA.

²Center for Computational Science and Engineering, Massachusetts Institute of Technology, 77 Massachusetts Ave, Cambridge, MA, 02139, USA.

³Department of Materials Science and Engineering, Massachusetts Institute of Technology, 77 Massachusetts Ave, Cambridge, MA, 02139, USA.

⁴Department of Nuclear Science and Engineering, Massachusetts Institute of Technology, 77 Massachusetts Ave, Cambridge, MA, 02139, USA.

⁵Lincoln Laboratory, Massachusetts Institute of Technology, 244 Wood St, Lexington, MA, 02421, USA.

*Corresponding author(s). E-mail(s): rafagb@mit.edu;

Abstract

Understanding material surfaces and interfaces is vital in applications like catalysis or electronics. *Ab initio* simulations, combining energies from electronic structure with statistical mechanics, can, in principle, predict the structure of material surfaces as a function of thermodynamic variables. However, accurate energy simulations are prohibitive when coupled to the vast phase space that must be statistically sampled. Here, we present a bi-faceted computational loop to predict surface phase diagrams of multi-component materials that accelerates both the energy scoring and statistical sampling methods. Fast, scalable, and data-efficient machine learning interatomic potentials are trained on high-throughput density-functional theory calculations through closed-loop active learning. Markov-chain Monte Carlo sampling in the semi-grand canonical ensemble is enabled by using virtual surface sites. The predicted surfaces for GaN(0001) and SrTiO₃(001) are in agreement with past work and suggest that the proposed strategy can model complex material surfaces and discover previously unreported surface terminations.

Keywords: neural network force field, active learning, Markov-chain Monte Carlo, semi-grand canonical ensemble, density-functional theory

1 Introduction

Surface structure determines the properties and performance of materials in application areas such as heterogeneous catalysis [1, 2], electrocatalysis [3–5], or electrochemical energy storage [6–8]. Material surfaces are not just pristine cuts of the bulk structure, and even for a single surface facet, equilibrium reconstruction can lead to vastly different terminations and patterns as a function of temperature, external chemical potentials, and applied electrical potential [9–13]. Experimental methods for studying surfaces at the atomic level are costly and involved so they cannot cover the wide range of experimental conditions [13, 14].

Simulations have the potential to capture complex surface structures at a wide range of external conditions. To do so, accurate and computationally affordable surface energy predictions are needed, along with efficient statistical sampling across surface compositions and configurations. On the energy modelling front, while classical interatomic force fields with few fitted parameters are sufficient for simple surfaces such as those of Au and GaN [15, 16], they are unsuited for multi-component surfaces that cannot be modeled accurately with simple functional forms.

Accurate computational studies of complex surfaces have relied on energetics derived from expensive density-functional theory (DFT) simulations of human-input guess surfaces, but this strategy does not easily scale to the diversity of possible structures. Kolpak *et al.* manually constructed candidate surfaces of BaTiO₃(001) with various coverage levels comprising vacancies and adsorbates of Ba, Ti, and O as well as Ti_xO_y or Ba_xO_y layers based on chemical intuition and previous experimental data [17]. Then, they used DFT relaxations to produce a phase diagram that connected external conditions to surface structures. Nevertheless, human intuition does not guarantee sufficient exploration of the phase space to uncover the most thermodynamically stable structures [18], as demonstrated by an unexpected α -Boron(111) surface reconstruction [19].

More principled sampling strategies systematically improve the generalizability of these computations and their ability to find unexpected phases, but they lead to trade-offs among the size of phase space explored, the energy accuracy, and computational cost. Wexler *et al.* overcame the limitations of human-input structures at the cost of relying on sample-intense grand canonical Monte Carlo (MC) sampling of the Ag(111) surface and expensive DFT calculations at every MC iteration [18]. Hess and Yildiz reduced the cost of energy calculations by using electrostatic energy computed from Bader charges instead and used canonical MC to limit the phase space [20]. In their study of La_{0.75}Sr_{0.25}MnO₃(001) (LSM25), Hess and Yildiz only optimized the lowest-energy structures obtained from MCMC at the DFT level. However, since electrostatic energies are not high-fidelity estimates of true energies, the final structures were not guaranteed to be the most stable.

Machine learning (ML) force fields are much faster than DFT calculations while preserving accuracy [21, 22] but they have not been connected to an efficient sampling scheme to explore the phase space of multi-component surfaces in a heuristic-free fashion. Recent works have proposed reconstruction pipelines utilizing ML force fields, but they still require guess compositions and do not consider the influence of external conditions. Merte *et al.* studied oxidation of Pt₃Sn [14] using Gaussian process regression as the energy model and a genetic algorithm for sampling the configurational space, but surface compositions were manually constructed. A similar workflow based on a neural network force field (NFF) was developed by Madsen and co-workers to analyze fixed compositions of SrTiO₃(110) [23]. ML-based sampling

methods that allow surface compositions to vary are limited to one adsorbate type on mono-component surfaces with less efficient sampling schemes. An example is the work of Xu *et al.* studying oxygen adsorption on Pt surfaces with grand canonical MC [24].

We present our Heuristic-Free Surface Reconstruction (HFSurfRecon) framework, which achieves thorough statistical sampling of thermodynamic states and avoids relying on hand-picked trial surfaces while being computationally efficient. HFSurfRecon utilizes ML force fields and active learning (AL) to enable fast and accurate energetics. In addition, because surface reconstruction typically takes place on sites that emerge from the underlying slab, we utilize the computationally efficient Virtual Surface Site Relaxation-Monte Carlo (VSSR-MC) sampling algorithm in the semi-grand canonical ensemble, instead of the more intensive grand canonical Monte Carlo. VSSR-MC samples across compositional and configurational search spaces to efficiently and accurately explore complex, stable surface structures across a range of external chemical potentials. To validate our semi-grand ensemble sampling strategy based on virtual sites, we recover a known reconstruction of the well-studied GaN(0001) surface using a classical force field. We then show the effectiveness of the full HFSurfRecon pipeline on SrTiO₃(001), a complex perovskite unsuited for classical force fields, using an NFF energy model. We demonstrate that our uncertainty-driven AL strategy working in tandem with VSSR-MC sampling acquires new DFT data points only at relevant regions of the surface phase space. In fewer than 5000 DFT single-point calculations, the NFF can be trained to obtain accurate energy predictions for many distinct chemical compositions. Finally, we construct an SrTiO₃(001) surface phase diagram that compares well with literature results and reveals new low-energy surface terminations. Our algorithm can be easily applied to any surface of interest and paves the way to study unknown multi-component materials under challenging environments such as in aqueous electrochemistry.

2 Results

2.1 Development of the end-to-end heuristic-free framework

Fig. 1 shows our HFSurfRecon computational workflow. Starting solely with a clean-cut surface and algorithmically generated virtual adsorption sites as inputs (see Section 4.2), a surface phase diagram is produced. In this workflow, VSSR-MC sampled structures have the dual purpose of improving the NFF energy model and obtaining surface reconstruction statistics, further improving the efficiency of our pipeline.

The phase diagram is obtained through successive surface reconstruction runs that, starting with the pristine surface as input, explore the surface phase space using VSSR-MC. Runs are conducted at different external conditions such as pressure, species chemical potential, and applied electrical potential.

Every individual VSSR-MC sampling iteration starts with discretely choosing one elemental identity at a selected adsorption site. A key innovation in VSSR-MC is that empty sites are defined as virtual atoms thus avoiding the higher volume space of grand canonical sampling in Cartesian coordinates. As such, adding an atom or removing an existing atom become instances of changing elemental identity and close contacts corresponding to very high repulsive energies can be easily rejected based on hard-sphere cutoffs. VSSR-MC is advantageous because its trials are limited to high-likelihood virtual sites responsible for reconstructions that relate to the symmetry of

the pristine slab. A disadvantage is that it is focused on thin, periodic reconstructions and will struggle to reconstruct amorphized thicker slabs, which do not follow virtual site geometries.

Following discrete sampling, all adsorbates and surface atoms undergo continuous relaxation of atomic positions away from their assigned sites by gradient descent, allowing us to efficiently explore the vast configurational space. The energy model used is a classical force field for mono- and bi-component materials or a machine-learned force field model for complex materials. The structure obtained after discrete sampling and continuous relaxation is evaluated with the acceptance criterion corresponding to the semi-grand canonical ensemble [25, 26]:

$$P = \min \left\{ 1, \exp \left(-\frac{\Delta E_{\text{slab}} - \Delta \mu}{k_B T} \right) \right\} \quad (1)$$

where ΔE_{slab} is the change in slab energy after both discrete sampling and continuous relaxation, $\Delta \mu$ is the change in chemical potential due to discrete sampling, k_B is the Boltzmann constant, and T is the sampling temperature.

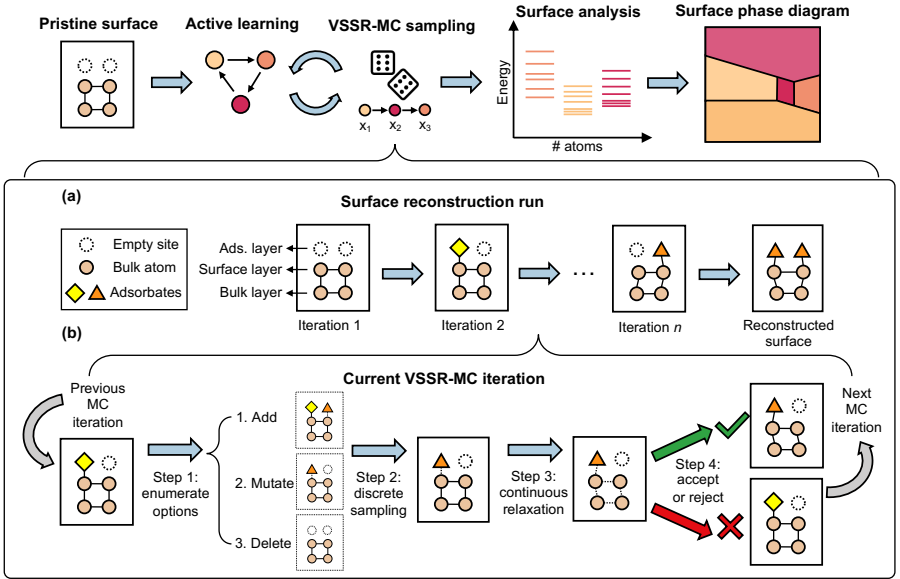


Fig. 1 Heuristic-Free Surface Reconstruction (HFSurfRecon) framework. (a) The proposed surface reconstruction process consists of multiple iterations of VSSR-MC. Starting from the initial pristine surface with empty adsorption sites, a series of iterations alter both the atomic identities at adsorption sites and the relative atomic positions within the structure. (b) In each VSSR-MC iteration, there are three steps. Starting from a surface taken from the previous iteration, in step 1, possible options for discrete sampling on a single adsorption site are enumerated. The possible actions are: add, replace, and remove. In step 2, the chosen discrete sampling action is performed to produce a candidate structure. This mutation is followed by continuous relaxation in step 3. For step 3, an energy model is required, such as a classical force field or a neural network force field. Finally, in step 4, the candidate structure is evaluated using an MC acceptance criterion.

We also developed an active learning (AL) strategy (Fig. 2) to efficiently acquire the fewest possible DFT-evaluated structures required for NFF training. At each AL iteration, we train an ensemble of neural force field (NFF) models for uncertainty quantification [27, 28] (see Section 4.3). To iteratively select structures for DFT evaluation, we use uncertainty-based adversarial attack [29] or the newly developed VSSR-MC, combined with latent space clustering to seek out structures that maximize NFF prediction error, which in practice is estimated by the predicted force standard deviation (SD) (see Section 4.4). The adversarial attack algorithm displaces atomic positions of existing structures to regions of high SD but not high energy [29], thereby improving the accuracy and stability of the force field [30]. However, adversarial attacks cannot autonomously sample different compositions. VSSR-MC samples both new compositions and configurations across chemical potentials and guides the NFF to learn only relevant subsets of the vast phase space. At the same time, clustering candidate structures reduces the number of training data by only selecting those whose local chemical environments are unique [31].

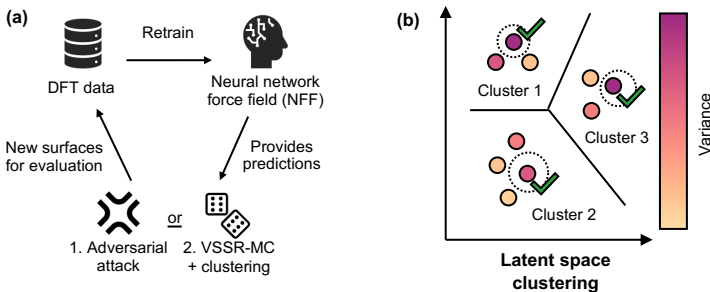


Fig. 2 Active learning (AL) procedure for neural network force field (NFF). (a) An initial ensemble of NFF models is trained using a common set of available DFT data. Using the NFF to provide predictions of forces, energies and their standard deviations (SD), either adversarial attack or VSSR-MC with latent space clustering is used to generate new surfaces for DFT evaluation. After performing DFT calculations on these new structures, they are added to the data pool and the NFF is retrained. (b) Latent space clustering procedure for MC-generated structures. Structures are clustered according to the first few principal components of latent space embeddings and the structure with the highest force SD in each cluster is selected for DFT evaluation.

2.2 GaN(0001) reconstruction with classical potential

To demonstrate our VSSR-MC sampling method, we investigated the reconstruction of the GaN(0001) surface. GaN is a well-studied semiconductor and the (0001) surface was described to have a contracted adsorption layer from DFT modeling [32]. A classical force field was used in our work [16] and several reconstructions matching the literature were obtained (Fig. 3). When viewed from the top, our structure in Fig. 3(a) shows the same rhombus patterns as the literature structure. The adsorbate distance from the pristine surface layer matched the literature value of 2.42 Å (side view, Fig. 3(b)) and the energy difference stood at a mere 0.008 meV/atom. The energy approached the ground state and VSSR-MC acceptance rate neared 0 at around 20,000 to 25,000 iterations in Fig. 3(c). Additional reconstructed surfaces can be found in Figure C1.

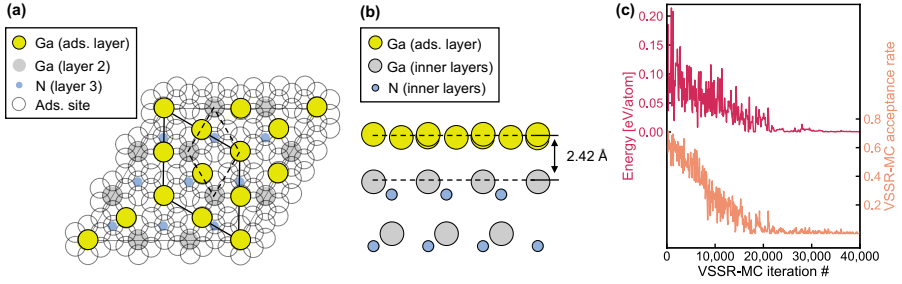


Fig. 3 Obtaining the GaN(0001) contracted-monolayer surface reconstruction using VSSR-MC and a classical potential. (a) Top view of surface reconstruction. Only the first three layers are shown. Our structure is visually identical to the literature optimized structure from Northrup *et al.* [32] with an energy difference of 0.008 meV/atom. (b) Side view of reconstructed surface. The average distance of the first two layers is 2.42 Å, in agreement with literature. (c) Typical VSSR-MC run profile for GaN(0001). Annealing from a high temperature allows convergence to a low-energy structure.

2.3 SrTiO₃(001) reconstructions with neural network force field

We validated the performance of our full HFSurfRecon framework on a challenging surface for which there is no known analytical potential. We chose SrTiO₃(001) because SrTiO₃ is representative of the complex perovskite oxide family and the (001) surface, in particular, is stable and demonstrates a variety of surface reconstruction patterns under different elemental chemical potentials [9–12].

2.3.1 Active learning for neural network force field

Including the initial dataset, active learning (AL) was run for a total of six iterations (see Section 4.4 for details) on SrTiO₃(001) slabs of varying compositions (example in Fig. 4(a)). A total of 6500 structures were generated: the first and last AL generations resulted in about 1500 structures each while AL generations 2–5 yielded approximately 800 structures each. Across our AL runs, we found a good correlation between force mean absolute error (MAE) and predicted force standard deviation (SD), demonstrating the validity of our error estimation procedure. Fig. 4(b) shows one such correlation plot derived from the final NFF model and sixth-generation structures.

Fig. 4(c) shows a principal component analysis (PCA), 2D projection of all new surface structures generated through our active learning process. In order to create a consistent representation across generation, PCA was applied to NN embeddings from the last-generation model on the full dataset. In Fig. 4(c), we see a distinct pattern of VSSR-MC structures compared with the initial structures, with VSSR-MC structures evolving over generations 3–5 to show streaks. These patterns suggest with NFF improvement, VSSR-MC was able to more effectively sample structures corresponding to surface energy minima. We also observe a correlation of the predicted energy with the first two principal axes (see Section 4.3).

Fig. 4(d) shows the performance of the NFF model, measured by energy MAE and force MAE, after each AL iteration over a common test data. The force and energy MAE drop significantly within four AL iterations, suggesting the effectiveness of the AL process for sampling the most informative surfaces for ML model training. While

the overall trend of both MAEs is down, the increase in energy MAE during generation 2 can be attributed to the distribution mismatch between the starting structures and the MC-sampled structures, suggesting the first generation model was overfit to the initial dataset and struggled to generalize to the much broader and realistic phase space explore during the AL cycles. The decrease from generation 3 to 4 was the most dramatic and in generation 4, an improved NFF allowed VSSR-MC samples to more closely follow the underlying distribution, resulting in the performance improvement. Overall, after dataset splitting, the final NFF was trained on fewer than 5000 structures and achieved a force MAE of 0.10 eV/Å and an energy MAE of 5.18 meV/atom (see Fig. C2) across the phase space needed to power production VSSR-MC runs.

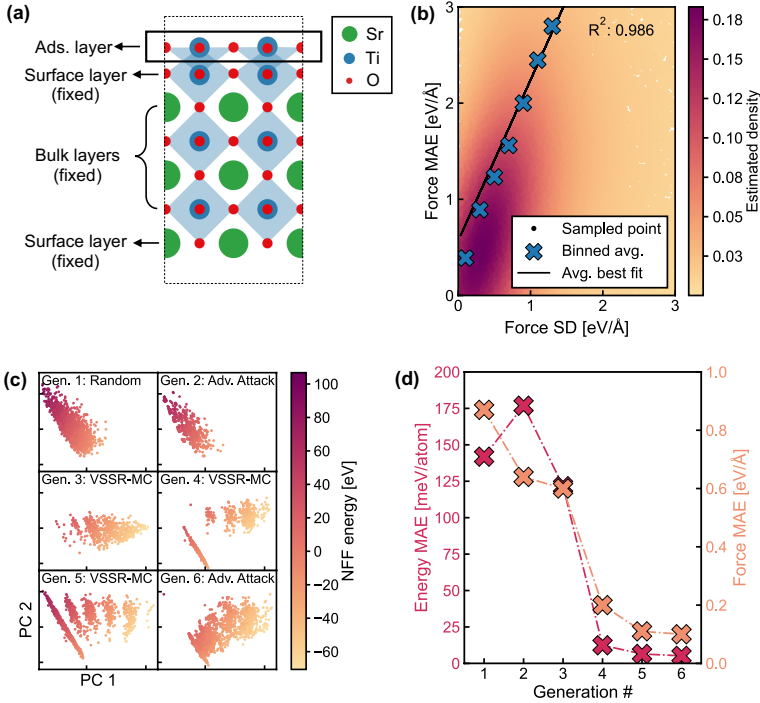


Fig. 4 Active learning for neural network force field. (a) Example SrTiO₃(001) surface for training NFF. The surface consists of an adsorption layer with variable chemical compositions and configurations, and inner layers with fixed compositions. (b) Correlation plot of force MAE with force SD. The trend implies that force SD is a fair surrogate for estimating force MAE. (c) Principal component analysis (PCA) of surfaces obtained at each AL generation. Starting with generation 2, a mix of adversarial attack and VSSR-MC with latent space clustering were used. (d) Retrospective performance of NFF trained using all surfaces available at each AL generation. Performance was measured using a test set consisting of VSSR-MC structures sampled from the 6th generation NFF model to reflect our use case.

2.3.2 Data analysis and constructing the phase diagram

We first present a summary of literature data on $\text{SrTiO}_3(001)$ reconstructions. The structure of $\text{SrTiO}_3(001)$ has inspired intensive research and debate. A double-layer (DL) TiO_2 -terminated surface is supported by both experiments and theory [11, 33, 34]. But single-layer (SL) TiO_2 and SL SrO terminations have also been reported [9, 10, 35, 36]. All these surfaces can be related to the chemical potential of the constitutive elements in the material bulk, which is assumed to be in equilibrium with the environment. In this case, the Sr chemical potential, μ_{Sr} , is the most relevant. By increasing μ_{Sr} , which can be achieved by evaporating Sr metal into the reaction environment, adding Sr to the surface becomes more favorable, resulting in the depletion of Ti and finally the formation of an SrO adlayer [9, 12].

In our surface reconstruction runs, we observed all three terminations starting from DL TiO_2 in low μ_{Sr} to SL TiO_2 (i.e., the unreconstructed surface) in intermediate μ_{Sr} , and SL SrO in high μ_{Sr} . A schematic is provided in Fig. 5(a) to illustrate this relationship. Due to our choice of modeling $\text{SrTiO}_3(001)$, there is a symmetrical relationship between μ_{Sr} and μ_{O} (Equation 6). Thus, no additional runs varying μ_{O} were necessary.

Analyzing our data obtained from VSSR-MC, we constructed a surface phase diagram of $\text{SrTiO}_3(001)$ in Fig. 5(b) that maps chemical potentials of Sr and O to the most stable surface terminations. Our phase diagram matches the expected trend in μ_{Sr} . It is also similar to the one obtained by Heifets *et al.* with a narrow strip of SL TiO_2 phase sandwiched between a DL TiO_2 phase at significant oxygen vacancies (low μ_{O}) and low μ_{Sr} , and a SL SrO phase at considerable Sr concentrations in an oxygen atmosphere (high μ_{O} and μ_{Sr}) [12]. We additionally assign three experimental $\text{SrTiO}_3(001)$ surfaces to our phase diagram, taking into account μ_{Sr} is loosely related to experimental procedures while μ_{O} can be calculated from p_{O_2} and the experimental temperature.

To construct the phase diagram, the surface free energy (Ω_{surf}) was recalculated for each structure using the final NFF model (see Section 4.5) at various μ_{Sr} and we plotted Ω_{surf} against the difference in the number of Sr and Ti atoms ($\Gamma_{\text{Sr}}^{\text{Ti}}$) for each slab. In the plots for $\mu_{\text{Sr}} = -10$ eV in Fig. 5(c), $\mu_{\text{Sr}} = -7$ eV in Fig. 5(d), and $\mu_{\text{Sr}} = -4$ eV in Fig. 5(e), we see that structures near the minimum Ω_{surf} correspond to the three known terminations. DL TiO_2 (Fig. 5(c)) and SL TiO_2 (Fig. 5(d)) had the lowest energy at $\mu_{\text{Sr}} = -10$ eV and $\mu_{\text{Sr}} = -7$ eV respectively. SL SrO (Fig. 5(e)) had the second lowest energy at $\mu_{\text{Sr}} = -4$ eV, and became the lowest after filtering for stoichiometry.

2.3.3 Comparing double-layer TiO_2 terminations

We additionally show that VSSR-MC faithfully recreated different reconstruction patterns of the DL TiO_2 surface. As reported by [11, 33] and others, DL TiO_2 does not consist of a single termination. 2×2 , 2×1 and 1×1 terminations are possible and we describe these terminations in Table 1. The most common 2×2 termination in literature is denoted in Table 1 as $2\times 2\text{-A}$. The dominant DL TiO_2 terminations could vary based on the exact surface structure and exchange-correlation functional, calculation settings, and empirical dispersion or Hubbard corrections. In this case, VSSR-MC samples contain two out of the three literature terminations: $2\times 2\text{-A}$ and 1×1 . These two TiO_2 terminations are close to one another in stability, as in [33].

The algorithm also discovered two surface terminations not previously reported, which we denote as $2\times 2\text{-B}$ and $2\times 2\text{-C}$. $2\times 2\text{-C}$ has a similar energy to the two observed

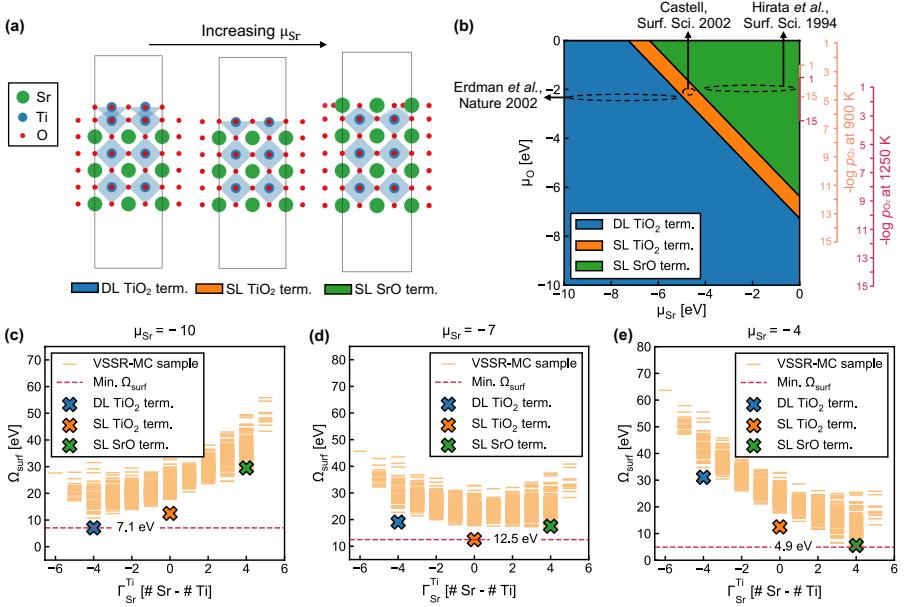


Fig. 5 Analyzing dominant SrTiO₃(001) surface terminations observed during VSSR-MC runs at different chemical potentials. (a) Side-view of change in dominant surface termination as μ_{Sr} increases. (b) Computed phase diagram showing the stable surface terminations at varying μ_{Sr} and μ_{O} along with estimated positions of three experimental SrTiO₃(001) surfaces. (c-e) Surface free energy (Ω_{surf}) plots of sampled structures as a function of the difference in the number of Sr and Ti atoms. Plots shown correspond to Ω_{surf} at various μ_{Sr} : (c) $\mu_{\text{Sr}} = -10$ eV, (d) $\mu_{\text{Sr}} = -7$ eV, and (e) $\mu_{\text{Sr}} = -4$ eV. The minimum energy surfaces are crossed out and correspond to those from literature.

literature terminations but 2x2-B is lower in energy. The 2x1 reconstruction reported in the literature was not observed during surface reconstruction runs. Energy prediction using NFF and confirmed using DFT demonstrate an energy more than 2 eV above that of the most stable surface (2x2-B) and almost 1 eV above that of the next highest energy termination (2x2-C). We also observe the consistency between NFF predictions and DFT energies, which again shows the accuracy of NFFs as an energy model.

3 Discussion

Understanding interfacial chemical reactivity in thermo- and electro-catalysis, or in batteries requires an atomistic picture of the complex surfaces that they occur on. Despite the significant effect of surface structure on properties, traditional computational study of surfaces over a comprehensive range of conditions has proven difficult due to the trade-offs among simulation speed, energetic accuracy, and statistical coverage. Meanwhile, recent developments bringing in ML to surface reconstruction are promising but have either been limited to expensive sampling of few-component surfaces or required the input of guess structures for complex surfaces.

In this paper, we developed Heuristic-Free Surface Reconstruction that integrates Virtual Surface Site Relaxation-Monte Carlo sampling in the semi-grand canonical

<div><div><div><div><div></div><div>Ti</div></div><div><div></div><div>O</div></div></div></div><div><div><div><div></div><div>VSSR-MC</div></div><div><div></div><div>Literature</div></div></div></div></div>	Type	2x2-A	2x1	1x1	2x2-B	2x2-C
	Top Layer					
	Occurrence					
	DFT energy [eV]	1.116	2.422	1.306	0.000	1.442
	NFF energy [eV]	0.988 ± 0.050	2.218 ± 0.344	0.948 ± 0.139	0.000 ± 0.151	1.139 ± 0.124

Table 1 Comparing DFT and NFF energies of double-layer (DL) TiO_2 terminations, all with the same composition. The NFF predicted energies are close to DFT energies. Additionally, the previously-unreported 2x2-B and 2x2-C terminations have roughly equal or lower energies than those of the other three literature-reported surfaces.

ensemble, neural network force field, and active learning for prior-free simulations of complex surfaces. As a test case, we showed the validity of VSSR-MC sampling with a classical potential by recovering the contracted-monolayer reconstruction of the semiconductor GaN(0001). Next, we proved the ability of the full HFSurfRecon procedure to sample stable terminations across compositions and configurations of the catalytically-relevant $\text{SrTiO}_3(001)$ with an NFF. Our framework built the surface phase diagram of $\text{SrTiO}_3(001)$ starting from the pristine surface without preconceptions about the structure of the system and revealed new termination patterns, including a lowest-energy state confirmed by higher quality DFT simulations. By introducing an AL procedure that takes advantage of MC samples, improving the force field and mapping out the surface phase diagram were performed concurrently, allowing for efficient use of compute time and data.

In this work, we sampled only one adsorption layer. Future work would benefit from an improved understanding of complex surface reconstructions as results of stoichiometric changes across multiple adsorption layers, or to vacancies in the bulk. Highly amorphized absorbate layers will likely occur off the virtual sites used by VSSR-MC and would need to be addressed with more sample-intensive grand canonical Monte Carlo in 3D space. While our approach is not strictly constrained by the size of the unit cell, for $\text{SrTiO}_3(001)$ especially, we chose to use a relatively small unit cell whereas larger ones could show more complex reconstruction patterns. Additionally, there is a wide literature of $\text{SrTiO}_3(001)$ reconstructions and not all past studies agree with each other. Further experimental studies probing different combinations of chemical potentials will help validate our phase diagram. Finally, we also acknowledge that MCMC-based sampling is difficult to parallelize and we envision an ML-based sampling method in the future to improve sampling speed.

Nevertheless, our algorithm is a general method that can be applied to complex, multi-component surfaces and adapted to challenging aqueous environments and electrical potentials that current experimental and computational efforts have not been able to address.

4 Methods

4.1 Virtual Surface Site Relaxation-Monte Carlo

The Metropolis-Hastings MCMC algorithm was adapted to implement VSSR-MC. VSSR-MC simulations were performed in the canonical ensemble in addition to the semi-grand ensemble. In the canonical ensemble simulation, the number of each adsorbate type is fixed. For each canonical VSSR-MC iteration, a pair of adsorption sites are chosen such that the number of adsorbates do not change. In the semi-grand ensemble simulation, the chemical potentials of adsorbates are supplied and the total number of adsorbates may vary across a MC run. For each semi-grand VSSR-MC iteration, one adsorption site is randomly chosen to change state.

For GaN(0001), the semi-grand ensemble method was first used with $\mu_{\text{Ga}} = 5$ eV to increase the number of Ga adsorbates to 12 before switching over to the canonical ensemble for annealing with annealing parameter $\alpha = 0.99$. For SrTiO₃(001), semi-grand VSSR-MC was run at various μ_{Sr} and a sampling temperature of at least 1000K. (See 4.4 for details.) Following the discrete sampling step, continuous relaxation was performed using the conjugate gradient method in LAMMPS [37] (for the adsorbate atoms in GaN(0001)) or the BFGS algorithm in ASE [38] (for both surface and adsorbate atoms in SrTiO₃(001)). The chemical potential of virtual surface sites is set to 0 eV.

For each iteration in the canonical ensemble, the acceptance probability P is given by the minimum of unity and the ratio of the Boltzmann weights between the proposed and current state:

$$P = \min \left\{ 1, \exp \left(-\frac{\Delta E_{\text{slab}}}{k_B T} \right) \right\} \quad (2)$$

where ΔE_{slab} is the change in slab energy after both discrete and continuous sampling, k_B is the Boltzmann constant, and T is the sampling temperature.

4.2 Surface slab modeling

The Python ASE, CatKit [39], and pymatgen [40] libraries were used to create and manipulate surfaces as well as to generate virtual adsorption sites. VESTA was used for visualization and producing figures [41].

4.2.1 GaN(0001) slab modeling

A GaN hexagonal unit cell from the Materials Project [42] (mp-804) was cut in the (0001) plane to form a 3x3 lattice with two layers. A vacuum spacing of 15 Å in total was added to the ends of the slab. Overlapping adsorption sites (~ 100) were defined up to 2.00 Å from the Ga-terminating surface using the pymatgen `AdsorbateSiteFinder` class. This class creates adsorption sites using a Delaunay triangulation-based algorithm. For this surface, Ga was the only adsorbate.

4.2.2 SrTiO₃(001) slab modeling

An SrTiO₃ cubic unit cell from the Materials Project (mp-5229) was optimized and cut in the (001) plane to create a 2x2 lattice with three layers of TiO₂ and SrO. A vacuum spacing of 15 Å in total was set at the ends of the slab. Overlapping

adsorption sites (~ 100) were defined at 1.55 Å from the TiO_2 surface using the same pymatgen `AdsorbateSiteFinder` class. For this surface, Sr, Ti, and O were possible adsorbates.

4.3 Neural network force field

NFFs for $\text{SrTiO}_3(001)$ were trained using an internal implementation of the equivariant PaiNN architecture [43]. The NFF energies are not the same as surface free energies (as in Section 4.5). A linear interpolation was performed over the lowest DFT energy structure for each composition to derive the energy offset per atom type. The corresponding atomic energy offset was subtracted from each atom in all structures to produce the target NFF energies. The original network hyperparameters were determined with SigOpt [44] to provide good results and thus unmodified. Briefly, the interaction cutoff between atoms was 5.0 Å, feature dimension was 128, number of radial basis functions was 20, and number of convolutions, 3. The swish activation function was employed [45]. Loss function was a weighted sum of the mean-squared errors of forces and energy in the 100:1 ratio. The Adam optimizer [46] was used with a starting learning rate (LR) of 0.001, an LR patience of 15 steps, and an LR decay factor of 0.3. A stopping potential in the form of $V = (\frac{\sigma}{\tau})^{12}$ was also employed. An ensemble of three NFF models was trained for 500 epochs each to provide energy and force estimates, and respective variances.

4.4 Active learning

To create the starting $\text{SrTiO}_3(001)$ dataset, Sr, Ti, and O adsorbates were randomly added to adsorption site, using a minimum distance of 1.5 Å between atoms to prevent non-physical results.

In further AL iterations, either adversarial attack or latent space clustering was used to obtain more surface geometries. Adversarial attack was implemented by Schwalbe-Koda *et al.* [29] with the adversarial objective given by:

$$\max_{\delta} \mathcal{L}_{\text{adv}}(X, \delta; \theta) = \max_{\delta} p(X_{\delta}) \sigma_F^2(X_{\delta}) \quad (3)$$

where \mathcal{L}_{adv} refers to the adversarial loss, X refers to starting atomic positions, δ refers to atomic displacements from starting positions, θ indicates that a neural network is used to estimate \mathcal{L}_{adv} . The objective means to perturb coordinates by a particular δ to maximise the predicted Boltzmann probabilities $p(X_{\delta})$ and variance of predicted forces $\sigma_F^2(X_{\delta})$. Adversarial attack was run at the default parameters of temperature $k_B T_{\text{adv}} = 0.7$ eV and adversarial LR = 5×10^{-4} for a total of 100 epochs. For the second-generation structures obtained using adversarial attack, the starting structures (seeds) were selected randomly. For the sixth-generation structures, seeds had a maximum energy of 1000 kcal/mol above the lowest energy structure.

Active learning using latent space clustering was done by first running VSSR-MC sampling from $\mu_{\text{Sr}} = -12$ eV to $\mu_{\text{Sr}} = 0$ eV in increments of 2. The MC-generated structures were clustered according to the first three principal components ($\sim 90\%$ explained variance) of their NFF embeddings and the most uncertain structure for each cluster was selected. An visualization of the clusters is given in Fig. C3(a).

Including starting structures, AL was run for a total of six generations. The second AL generation used adversarial attack to create a stable NFF for continuous relaxation. The next three generations (3-5) employed VSSR-MC with latent space

clustering to train our NFF in the phase space most relevant to surface reconstruction. The goal of using adversarial attack for the final AL generation was to make the force field more robust for low-energy structures.

4.5 Surface stability analysis

The analysis method is outlined below, details are in Appendix B. $\text{SrTiO}_3(001)$ surfaces were compared using the surface Gibbs free energy $\Omega_{\text{surf}}^{\text{SrTiO}_3}$ [12]:

$$\Omega_{\text{surf}}^{\text{SrTiO}_3} = G_{\text{slab}} - N_{\text{Sr}}\mu_{\text{Sr}} - N_{\text{Ti}}\mu_{\text{Ti}} - N_{\text{O}}\mu_{\text{O}} \quad (4)$$

where G_{slab} refers to Gibbs free energy of the slab. For each element a , N_a refers to the number of a atoms in the slab, μ_a refers to the chemical potential of a .

By the following relationship:

$$\mu_{\text{SrTiO}_3} = \mu_{\text{Sr}} + \mu_{\text{Ti}} + 3\mu_{\text{O}} = g_{\text{SrTiO}_3}^{\text{bulk}}$$

where $g_{\text{SrTiO}_3}^{\text{bulk}}$ refers to the Gibbs free energy of the SrTiO_3 unit cell. We obtain:

$$\Omega_{\text{surf}}^{\text{SrTiO}_3} = G_{\text{slab}} - N_{\text{Ti}}g_{\text{SrTiO}_3}^{\text{bulk}} - \Gamma_{\text{Sr}}^{\text{Ti}}\mu_{\text{Sr}} - \Gamma_{\text{O}}^{\text{Ti}}\mu_{\text{O}} \quad (5)$$

where $\Gamma_a^{\text{Ti}} = N_a - N_{\text{Ti}}\frac{N_a^{\text{bulk}}}{N_{\text{Ti}}^{\text{bulk}}}$ refers to the excess a component in the surface with respect to the number of Ti atoms and $\frac{N_a^{\text{bulk}}}{N_{\text{Ti}}^{\text{bulk}}}$ refers to the bulk stoichiometric ratio of a to Ti.

Approximating Gibbs free energy by DFT energies [47, 48] and redefining chemical potentials by subtracting reference state energies E_a for component a obtained from DFT calculations:

$$\Omega_{\text{surf}}^{\text{SrTiO}_3} = \phi - \Gamma_{\text{Sr}}^{\text{Ti}}\mu_{\text{Sr}} - \Gamma_{\text{O}}^{\text{Ti}}\mu_{\text{O}} \quad (6)$$

where

$$\phi \approx E_{\text{slab}} - N_{\text{Ti}}E_{\text{SrTiO}_3}^{\text{bulk}} - \Gamma_{\text{Sr}}^{\text{Ti}}E_{\text{Sr}}^{\text{bulk}} - \Gamma_{\text{O}}^{\text{Ti}}\frac{E_{\text{O}_2}}{2}$$

and as a result, $\mu_{\text{Sr}} < 0$, $\mu_{\text{O}} < 0$ for thermodynamic stability.

VSSR-MC samples according to the grand potential Ω_{G} , which is equivalent to Ω_{surf} after approximations:

$$\begin{aligned} \Omega_{\text{G}}^{\text{SrTiO}_3} &= E_{\text{slab}} - Ts_{\text{slab}} - N_{\text{Sr}}\mu_{\text{Sr}} - N_{\text{Ti}}\mu_{\text{Ti}} - N_{\text{O}}\mu_{\text{O}} \\ &\approx G_{\text{slab}} - N_{\text{Sr}}\mu_{\text{Sr}} - N_{\text{Ti}}\mu_{\text{Ti}} - N_{\text{O}}\mu_{\text{O}} \\ &= \Omega_{\text{surf}}^{\text{SrTiO}_3} \end{aligned} \quad (7)$$

where s_{slab} is the slab entropy.

4.6 Phase diagram creation

SrTiO_3 has three elements but only two degrees of freedom in chemical potential as in Equation 6. The chemical potential of virtual sites is fixed. The MC-sampled structures exhibit different $\Omega_{\text{surf}}^{\text{SrTiO}_3}$ as μ_{Sr} and μ_{O} change. By selecting the most stable structure at each μ_{Sr} and μ_{O} , a 2D phase diagram with μ_{Sr} and μ_{O} axes was obtained.

4.7 Density-functional theory calculations

Vienna *ab initio* Simulation Package (VASP) v.6.2.1 [49, 50] was employed to relax bulk structures and for single-point DFT calculations of $\text{SrTiO}_3(001)$ surfaces, using the projector augmented-wave (PAW) method to describe core electrons [51, 52]. The Perdew-Burke-Ernzerhof (PBE) functional within the generalized-gradient approximation (GGA) were utilized [53] along with the Hubbard U correction [54] for spin-polarized calculations. Dipole corrections to the total energy were enabled along the z-axis. The kinetic energy cutoff for plane waves was set to 520 eV. In the self-consistent field cycle, a limit of 10^{-6} eV was adopted as the stopping criterion.

4.8 Workflow management and compute time

An internal library, HTVS (for high-throughput virtual simulations) managed the DFT calculations, NFF training, and adversarial attack. VSSR-MC and latent space clustering were run in separate procedures. DFT calculations took about 0.5-1 hour each on 30 cores of an Intel Xeon Platinum 8260 CPU. NFF training increased with dataset size and approached a maximum of 3 hours per model with an Nvidia Volta V100 32GB GPU. VSSR-MC runs sampled at a rate of about an hour per 10,000 iterations using the NFF energy model ($\sim 20,000$ iterations for each run for $\text{SrTiO}_3(001)$) and about 15 minutes per 10,000 iterations using the classical Tersoff potential ($\sim 50,000$ iterations for each run for $\text{GaN}(0001)$). Adversarial attack and latent space clustering were comparatively fast, taking less than 15 minutes for each generation.

5 Data availability

The trained models, DFT data, and code used for data analysis are available on Zenodo: <https://zenodo.org/record/7927039>.

6 Code availability

The algorithm reported in this work is available on GitHub: <https://github.com/learningmatter-mit/surface-sampling>.

7 Acknowledgments

DISTRIBUTION STATEMENT A. Approved for public release. Distribution is unlimited. This material is based upon work supported by the Under Secretary of Defense for Research and Engineering under Air Force Contract No. FA8702-15-D-0001. Any opinions, findings, conclusions or recommendations expressed in this material are those of the author(s) and do not necessarily reflect the views of the

Under Secretary of Defense for Research and Engineering. © 2023 Massachusetts Institute of Technology. Delivered to the U.S. Government with Unlimited Rights, as defined in DFARS Part 252.227-7013 or 7014 (Feb 2014). Notwithstanding any copyright notice, U.S. Government rights in this work are defined by DFARS 252.227-7013 or DFARS 252.227-7014 as detailed above. Use of this work other than as specifically authorized by the U.S. Government may violate any copyrights that exist in this work.

The authors thank Gavin Winter, Jiayu Peng and Nathan Frey for helpful discussions. The authors also appreciate manuscript editing by Jiayu Peng and Alexander Hoffman. XD acknowledges support from the National Science Foundation Graduate Research Fellowship under Grant No. 2141064. J.K.D. was supported by the Department of Defense through the National Defense Science & Engineering Graduate Fellowship Program. The authors are grateful for computation time allocated on the MIT SuperCloud cluster, MIT Engaging cluster, and the NERSC Perlmutter cluster.

8 Competing interests

The authors declare no competing financial or non-financial interests.

9 Author’s contributions

X.D. implemented the sampling algorithm, performed surface modeling, ran DFT calculations, trained the neural networks, and carried out surface stability analysis. J.K.D. assisted with sampling algorithm implementation and provided guidance with surface modeling. J.R.L. provided guidance with surface modeling and ran DFT calculations. R.M. provided guidance with neural network training and active learning. B.Y. provided guidance with the choice of surfaces and surface stability analysis. L.L. supervised the research and contributed to securing funding. R.G.-B. conceived the project, supervised the research and contributed to securing funding. All contributed to results discussion and manuscript writing.

References

- [1] Shi, R., Waterhouse, G.I.N., Zhang, T.: Recent Progress in Photocatalytic CO₂ Reduction Over Perovskite Oxides. *Solar RRL* **1**(11), 1700126 (2017). <https://doi.org/10.1002/solr.201700126>. _eprint: <https://onlinelibrary.wiley.com/doi/pdf/10.1002/solr.201700126>. Accessed 2023-03-05
- [2] Sumaria, V., Nguyen, L., Tao, F.F., Sautet, P.: Atomic-Scale Mechanism of Platinum Catalyst Restructuring under a Pressure of Reactant Gas. *Journal of the American Chemical Society* **145**(1), 392–401 (2023). <https://doi.org/10.1021/jacs.2c10179>. Publisher: American Chemical Society. Accessed 2023-03-04
- [3] Fabbri, E., Nachtegaal, M., Binninger, T., Cheng, X., Kim, B.-J., Durst, J., Bozza, F., Graule, T., Schäublin, R., Wiles, L., Pertoso, M., Danilovic, N., Ayers, K.E., Schmidt, T.J.: Dynamic surface self-reconstruction is the key of highly active perovskite nano-electrocatalysts for water splitting. *Nature*

- Materials **16**(9), 925–931 (2017). <https://doi.org/10.1038/nmat4938>. Number: 9 Publisher: Nature Publishing Group. Accessed 2023-03-05
- [4] Zhang, Z., Wei, Z., Sautet, P., Alexandrova, A.N.: Hydrogen-Induced Restructuring of a Cu(100) Electrode in Electroreduction Conditions. *Journal of the American Chemical Society* **144**(42), 19284–19293 (2022). <https://doi.org/10.1021/jacs.2c06188>. Publisher: American Chemical Society. Accessed 2023-03-04
- [5] Sha, Z., Shen, Z., Calì, E., Kilner, J.A., Skinner, S.J.: Understanding surface chemical processes in perovskite oxide electrodes. *Journal of Materials Chemistry A* (2023). <https://doi.org/10.1039/D3TA00070B>. Publisher: The Royal Society of Chemistry. Accessed 2023-03-05
- [6] Jung, S.-K., Gwon, H., Hong, J., Park, K.-Y., Seo, D.-H., Kim, H., Hyun, J., Yang, W., Kang, K.: Understanding the Degradation Mechanisms of LiNi_{0.5}Co_{0.2}Mn_{0.3}O₂ Cathode Material in Lithium Ion Batteries. *Advanced Energy Materials* **4**(1), 1300787 (2014). <https://doi.org/10.1002/aenm.201300787>. eprint: <https://onlinelibrary.wiley.com/doi/pdf/10.1002/aenm.201300787>. Accessed 2023-03-05
- [7] Han, B., Key, B., Lapidus, S.H., Garcia, J.C., Iddir, H., Vaughey, J.T., Dogan, F.: From Coating to Dopant: How the Transition Metal Composition Affects Alumina Coatings on Ni-Rich Cathodes. *ACS Applied Materials & Interfaces* **9**(47), 41291–41302 (2017). <https://doi.org/10.1021/acsami.7b13597>. Publisher: American Chemical Society. Accessed 2023-03-05
- [8] Xu, C., Märker, K., Lee, J., Mahadevegowda, A., Reeves, P.J., Day, S.J., Groh, M.F., Emge, S.P., Ducati, C., Layla Mehdi, B., Tang, C.C., Grey, C.P.: Bulk fatigue induced by surface reconstruction in layered Ni-rich cathodes for Li-ion batteries. *Nature Materials* **20**(1), 84–92 (2021). <https://doi.org/10.1038/s41563-020-0767-8>. Number: 1 Publisher: Nature Publishing Group. Accessed 2023-03-05
- [9] Hirata, A., Saiki, K., Koma, A., Ando, A.: Electronic structure of a SrO-terminated SrTiO₃(100) surface. *Surface Science* **319**(3), 267–271 (1994). [https://doi.org/10.1016/0039-6028\(94\)90593-2](https://doi.org/10.1016/0039-6028(94)90593-2). Accessed 2023-03-23
- [10] Castell, M.R.: Scanning tunneling microscopy of reconstructions on the SrTiO₃(001) surface. *Surface Science* **505**, 1–13 (2002). [https://doi.org/10.1016/S0039-6028\(02\)01393-6](https://doi.org/10.1016/S0039-6028(02)01393-6). Accessed 2023-05-08
- [11] Erdman, N., Poeppelmeier, K.R., Asta, M., Warschkow, O., Ellis, D.E., Marks, L.D.: The structure and chemistry of the TiO₂-rich surface of SrTiO₃ (001). *Nature* **419**(6902), 55–58 (2002). <https://doi.org/10.1038/nature01010>. Number: 6902 Publisher: Nature Publishing Group. Accessed 2023-03-02
- [12] Heifets, E., Piskunov, S., Kotomin, E.A., Zhukovskii, Y.F., Ellis, D.E.: Electronic structure and thermodynamic stability of double-layered SrTiO₃ (001) surfaces: *Ab initio* simulations. *Physical Review B* **75**(11), 115417 (2007). <https://doi.org/10.1103/PhysRevB.75.115417>. Accessed 2023-02-22

- [13] Li, H., Jiao, Y., Davey, K., Qiao, S.-Z.: Data-Driven Machine Learning for Understanding Surface Structures of Heterogeneous Catalysts. *Angewandte Chemie* **135**(9), 202216383 (2023). <https://doi.org/10.1002/ange.202216383>. _eprint: <https://onlinelibrary.wiley.com/doi/pdf/10.1002/ange.202216383>. Accessed 2023-05-08
- [14] Merte, L.R., Bisbo, M.K., Sokolović, I., Setvín, M., Hagman, B., Shipilin, M., Schmid, M., Diebold, U., Lundgren, E., Hammer, B.: Structure of an Ultrathin Oxide on Pt₃Sn(111) Solved by Machine Learning Enhanced Global Optimization*. *Angewandte Chemie International Edition* **61**(25), 202204244 (2022). <https://doi.org/10.1002/anie.202204244>. _eprint: <https://onlinelibrary.wiley.com/doi/pdf/10.1002/anie.202204244>. Accessed 2023-03-04
- [15] Foiles, S.M., Baskes, M.I., Daw, M.S.: Embedded-atom-method functions for the fcc metals Cu, Ag, Au, Ni, Pd, Pt, and their alloys. *Physical Review B* **33**(12), 7983–7991 (1986). <https://doi.org/10.1103/PhysRevB.33.7983>. Publisher: American Physical Society. Accessed 2023-03-01
- [16] Nord, J., Albe, K., Erhart, P., Nordlund, K.: Modelling of compound semiconductors: analytical bond-order potential for gallium, nitrogen and gallium nitride. *Journal of Physics: Condensed Matter* **15**(32), 5649 (2003). <https://doi.org/10.1088/0953-8984/15/32/324>. Accessed 2023-02-20
- [17] Kolpak, A.M., Li, D., Shao, R., Rappe, A.M., Bonnell, D.A.: Evolution of the Structure and Thermodynamic Stability of the $\{\mathrm{BaTiO}\}_{-3}(001)$ Surface. *Physical Review Letters* **101**(3), 036102 (2008). <https://doi.org/10.1103/PhysRevLett.101.036102>. Publisher: American Physical Society. Accessed 2023-03-03
- [18] Wexler, R.B., Qiu, T., Rappe, A.M.: Automatic Prediction of Surface Phase Diagrams Using Ab Initio Grand Canonical Monte Carlo. *The Journal of Physical Chemistry C* **123**(4), 2321–2328 (2019). <https://doi.org/10.1021/acs.jpcc.8b11093>. Publisher: American Chemical Society. Accessed 2023-03-04
- [19] Zhou, X.-F., Oganov, A.R., Shao, X., Zhu, Q., Wang, H.-T.: Unexpected Reconstruction of the α -Boron (111) Surface. *Physical Review Letters* **113**(17), 176101 (2014). <https://doi.org/10.1103/PhysRevLett.113.176101>. Accessed 2023-03-17
- [20] Hess, F., Yildiz, B.: Polar or not polar? The interplay between reconstruction, Sr enrichment, and reduction at the $\{\mathrm{La}\}_{-0.75}\{\mathrm{Sr}\}_{-0.25}\{\mathrm{MnO}\}_{-3}$ (001) surface. *Physical Review Materials* **4**(1), 015801 (2020). <https://doi.org/10.1103/PhysRevMaterials.4.015801>. Publisher: American Physical Society. Accessed 2023-03-03
- [21] Unke, O.T., Chmiela, S., Sauceda, H.E., Gastegger, M., Poltavsky, I., Schütt, K.T., Tkatchenko, A., Müller, K.-R.: Machine Learning Force Fields. *Chemical Reviews* **121**(16), 10142–10186 (2021). <https://doi.org/10.1021/acs.chemrev.0c01111>. Publisher: American Chemical Society. Accessed 2023-03-05

- [22] Axelrod, S., Schwalbe-Koda, D., Mohapatra, S., Damewood, J., Greenman, K.P., Gómez-Bombarelli, R.: Learning Matter: Materials Design with Machine Learning and Atomistic Simulations. *Accounts of Materials Research* **3**(3), 343–357 (2022). <https://doi.org/10.1021/accountsmr.1c00238>. Publisher: American Chemical Society. Accessed 2023-05-09
- [23] Wanzenböck, R., Arrigoni, M., Bichelmaier, S., Buchner, F., Carrete, J., Madsen, G.K.H.: Neural-network-backed evolutionary search for SrTiO₃(110) surface reconstructions. *Digital Discovery* **1**(5), 703–710 (2022). <https://doi.org/10.1039/D2DD00072E>. Publisher: RSC. Accessed 2023-03-04
- [24] Xu, J., Xie, W., Han, Y., Hu, P.: Atomistic Insights into the Oxidation of Flat and Stepped Platinum Surfaces Using Large-Scale Machine Learning Potential-Based Grand-Canonical Monte Carlo. *ACS Catalysis* **12**(24), 14812–14824 (2022). <https://doi.org/10.1021/acscatal.2c03976>. Publisher: American Chemical Society. Accessed 2023-03-04
- [25] Bernardin, F.E., Rutledge, G.C.: Semi-Grand Canonical Monte Carlo (SGMC) Simulations to Interpret Experimental Data on Processed Polymer Melts and Glasses. *Macromolecules* **40**(13), 4691–4702 (2007). <https://doi.org/10.1021/ma062935r>. Accessed 2023-03-18
- [26] Damewood, J., Schwalbe-Koda, D., Gómez-Bombarelli, R.: Sampling lattices in semi-grand canonical ensemble with autoregressive machine learning. *npj Computational Materials* **8**(1), 1–10 (2022). <https://doi.org/10.1038/s41524-022-00736-4>. Number: 1 Publisher: Nature Publishing Group. Accessed 2023-03-18
- [27] Carrete, J., Montes-Campos, H., Wanzenböck, R., Heid, E., Madsen, G.K.H.: Deep Ensembles vs. Committees for Uncertainty Estimation in Neural-Network Force Fields: Comparison and Application to Active Learning. *arXiv. arXiv:2302.08805 [physics]* (2023). <https://doi.org/10.48550/arXiv.2302.08805>. <http://arxiv.org/abs/2302.08805> Accessed 2023-05-11
- [28] Tan, A.R., Urata, S., Goldman, S., Dietschreit, J.C.B., Gómez-Bombarelli, R.: Single-model uncertainty quantification in neural network potentials does not consistently outperform model ensembles. *arXiv. arXiv:2305.01754 [physics]* (2023). <http://arxiv.org/abs/2305.01754> Accessed 2023-05-09
- [29] Schwalbe-Koda, D., Tan, A.R., Gómez-Bombarelli, R.: Differentiable sampling of molecular geometries with uncertainty-based adversarial attacks. *Nature Communications* **12**(1), 5104 (2021). <https://doi.org/10.1038/s41467-021-25342-8>. Number: 1 Publisher: Nature Publishing Group. Accessed 2023-02-19
- [30] Fu, X., Wu, Z., Wang, W., Xie, T., Keten, S., Gomez-Bombarelli, R., Jaakkola, T.: Forces are not Enough: Benchmark and Critical Evaluation for Machine Learning Force Fields with Molecular Simulations. *arXiv. arXiv:2210.07237 [physics]* (2022). <http://arxiv.org/abs/2210.07237> Accessed 2023-05-09
- [31] Damewood, J., Karaguesian, J., Lunger, J.R., Tan, A.R., Xie, M., Peng, J.,

- Gómez-Bombarelli, R.: Representations of Materials for Machine Learning. arXiv. arXiv:2301.08813 [cond-mat] (2023). <https://doi.org/10.48550/arXiv.2301.08813>. <http://arxiv.org/abs/2301.08813> Accessed 2023-05-09
- [32] Northrup, J.E., Neugebauer, J., Feenstra, R.M., Smith, A.R.: Structure of GaN(0001): The laterally contracted Ga bilayer model. *Physical Review B* **61**(15), 9932–9935 (2000). <https://doi.org/10.1103/PhysRevB.61.9932>. Publisher: American Physical Society. Accessed 2023-02-27
- [33] Herger, R., Willmott, P.R., Bunk, O., Schlepütz, C.M., Patterson, B.D., Delley, B.: Surface of Strontium Titanate. *Physical Review Letters* **98**(7), 076102 (2007). <https://doi.org/10.1103/PhysRevLett.98.076102>. Publisher: American Physical Society. Accessed 2023-03-02
- [34] Hong, C., Zou, W., Ran, P., Tanaka, K., Matzelle, M., Chiu, W.-C., Markiewicz, R.S., Barbiellini, B., Zheng, C., Li, S., Bansil, A., He, R.-H.: Anomalous intense coherent secondary photoemission from a perovskite oxide. *Nature*, 1–3 (2023). <https://doi.org/10.1038/s41586-023-05900-4>. Publisher: Nature Publishing Group. Accessed 2023-03-09
- [35] Szot, K., Speier, W.: Surfaces of reduced and oxidized SrTiO_3 from atomic force microscopy. *Physical Review B* **60**(8), 5909–5926 (1999). <https://doi.org/10.1103/PhysRevB.60.5909>. Publisher: American Physical Society. Accessed 2023-03-07
- [36] Kubo, T., Nozoye, H.: Surface structure of $\text{SrTiO}_3(100)$. *Surface Science* **542**(3), 177–191 (2003). [https://doi.org/10.1016/S0039-6028\(03\)00998-1](https://doi.org/10.1016/S0039-6028(03)00998-1). Accessed 2023-03-07
- [37] Thompson, A.P., Aktulga, H.M., Berger, R., Bolintineanu, D.S., Brown, W.M., Crozier, P.S., in 't Veld, P.J., Kohlmeyer, A., Moore, S.G., Nguyen, T.D., Shan, R., Stevens, M.J., Tranchida, J., Trott, C., Plimpton, S.J.: LAMMPS - a flexible simulation tool for particle-based materials modeling at the atomic, meso, and continuum scales. *Computer Physics Communications* **271**, 108171 (2022). <https://doi.org/10.1016/j.cpc.2021.108171>. Accessed 2023-02-20
- [38] Larsen, A.H., Mortensen, J.J., Blomqvist, J., Castelli, I.E., Christensen, R., Dulak, M., Friis, J., Groves, M.N., Hammer, B., Hargus, C., Hermes, E.D., Jennings, P.C., Jensen, P.B., Kermode, J., Kitchin, J.R., Kolsbjerg, E.L., Kubal, J., Kaasbjerg, K., Lysgaard, S., Maronsson, J.B., Maxson, T., Olsen, T., Pastewka, L., Peterson, A., Rostgaard, C., Schiøtz, J., Schütt, O., Strange, M., Thygesen, K.S., Vegge, T., Vilhelmsen, L., Walter, M., Zeng, Z., Jacobsen, K.W.: The atomic simulation environment—a Python library for working with atoms. *Journal of Physics: Condensed Matter* **29**(27), 273002 (2017). <https://doi.org/10.1088/1361-648X/aa680e>. Publisher: IOP Publishing. Accessed 2023-02-14
- [39] Boes, J.R., Mamun, O., Winther, K., Bligaard, T.: Graph Theory Approach to High-Throughput Surface Adsorption Structure Generation. *The Journal of Physical Chemistry A* **123**(11), 2281–2285 (2019). <https://doi.org/10.1021/acs.jpca.9b00311>. Publisher: American Chemical Society. Accessed 2023-02-14

- [40] Ong, S.P., Richards, W.D., Jain, A., Hautier, G., Kocher, M., Cholia, S., Gunter, D., Chevrier, V.L., Persson, K.A., Ceder, G.: Python Materials Genomics (pymatgen): A robust, open-source python library for materials analysis. *Computational Materials Science* **68**, 314–319 (2013). <https://doi.org/10.1016/j.commatsci.2012.10.028>. Accessed 2023-02-14
- [41] Momma, K., Izumi, F.: VESTA 3 for three-dimensional visualization of crystal, volumetric and morphology data. *Journal of Applied Crystallography* **44**(6), 1272–1276 (2011). <https://doi.org/10.1107/S0021889811038970>. Number: 6 Publisher: International Union of Crystallography. Accessed 2023-03-07
- [42] Jain, A., Ong, S.P., Hautier, G., Chen, W., Richards, W.D., Dacek, S., Cholia, S., Gunter, D., Skinner, D., Ceder, G., Persson, K.A.: Commentary: The Materials Project: A materials genome approach to accelerating materials innovation. *APL Materials* **1**(1), 011002 (2013). <https://doi.org/10.1063/1.4812323>. Publisher: American Institute of Physics. Accessed 2023-02-14
- [43] Schütt, K., Unke, O., Gastegger, M.: Equivariant message passing for the prediction of tensorial properties and molecular spectra. In: *Proceedings of the 38th International Conference on Machine Learning*, pp. 9377–9388. PMLR, ??? (2021). ISSN: 2640-3498. <https://proceedings.mlr.press/v139/schutt21a.html> Accessed 2023-04-11
- [44] Martinez-Cantin, R., Tee, K., McCourt, M.: Practical Bayesian optimization in the presence of outliers. In: Storkey, A., Perez-Cruz, F. (eds.) *Proceedings of the Twenty-First International Conference on Artificial Intelligence And Statistics. Proceedings of Machine Learning Research*, vol. 84, pp. 1722–1731. PMLR, Playa Blanca, Lanzarote, Canary Islands (2018)
- [45] Ramachandran, P., Zoph, B., Le, Q.V.: Searching for Activation Functions. *arXiv*. arXiv:1710.05941 [cs] version: 2 (2017). <http://arxiv.org/abs/1710.05941> Accessed 2023-02-19
- [46] Kingma, D.P., Ba, J.: Adam: A Method for Stochastic Optimization. In: Bengio, Y., LeCun, Y. (eds.) *3rd International Conference on Learning Representations, ICLR 2015, San Diego, CA, USA, May 7-9, 2015, Conference Track Proceedings* (2015). <http://arxiv.org/abs/1412.6980> Accessed 2023-02-19
- [47] Reuter, K., Scheffler, M.: Composition, structure, and stability of $\text{RuO}_2(110)$ as a function of oxygen pressure. *Physical Review B* **65**(3), 035406 (2001). <https://doi.org/10.1103/PhysRevB.65.035406>. Publisher: American Physical Society. Accessed 2023-02-22
- [48] Heifets, E., Ho, J., Merinov, B.: Density functional simulation of the Ba Zr O₃ (011) surface structure. *Physical Review B* **75**(15), 155431 (2007). <https://doi.org/10.1103/PhysRevB.75.155431>. Accessed 2023-02-22
- [49] Kresse, G., Furthmüller, J.: Efficiency of ab-initio total energy calculations for metals and semiconductors using a plane-wave basis set. *Computational Materials Science* **6**(1), 15–50 (1996). [https://doi.org/10.1016/0927-0256\(96\)00008-0](https://doi.org/10.1016/0927-0256(96)00008-0). Publisher: Elsevier

- [50] Kresse, G., Furthmüller, J.: Efficient iterative schemes for ab initio total-energy calculations using a plane-wave basis set. *Physical Review B* **54**(16), 11169–11186 (1996). <https://doi.org/10.1103/PhysRevB.54.11169>. Publisher: American Physical Society
- [51] Blöchl, P.E.: Projector augmented-wave method. *Physical Review B* **50**(24), 17953–17979 (1994). <https://doi.org/10.1103/PhysRevB.50.17953>
- [52] Kresse, G., Joubert, D.: From ultrasoft pseudopotentials to the projector augmented-wave method. *Physical Review B* **59**(3), 1758–1775 (1999). <https://doi.org/10.1103/PhysRevB.59.1758>. Publisher: American Physical Society
- [53] Perdew, J.P., Burke, K., Ernzerhof, M.: Generalized Gradient Approximation Made Simple. *Physical Review Letters* **77**(18), 3865–3868 (1996). <https://doi.org/10.1103/PhysRevLett.77.3865>. Publisher: American Physical Society
- [54] Dudarev, S.L., Botton, G.A., Savrasov, S.Y., Humphreys, C.J., Sutton, A.P.: Electron-energy-loss spectra and the structural stability of nickel oxide: An LSDA+U study. *Physical Review B* **57**(3), 1505–1509 (1998). <https://doi.org/10.1103/PhysRevB.57.1505>. Publisher: American Physical Society. Accessed 2023-02-14
- [55] Allison, T.C.: NIST-JANAF Thermochemical Tables - SRD 13. National Institute of Standards and Technology (2013). <https://doi.org/10.18434/T42S31>. <https://janaf.nist.gov/> Accessed 2023-03-27

Appendix A Abbreviations used

The following is the list of abbreviation utilized.

- HFSurfRecon: Heuristic-Free Surface Reconstruction
- VSSR-MC: Virtual Surface Site Relaxation-Monte Carlo
- MCMC: Markov-chain Monte Carlo
- NFF: Neural network force field
- AL: Active learning
- ML: Machine learning
- DFT: Density-functional theory
- MAE: Mean absolute error
- SD: Standard deviation
- GA: Genetic algorithm
- GaN: Gallium nitride
- SrTiO₃: Strontium titanate
- SL: Single layer
- DL: Double layer

Appendix B Surface stability analysis

The stability of surfaces can be compared using the surface Gibbs free energy Ω_{surf} [12, 47, 48]:

$$\Omega_{\text{surf}} = G_{\text{slab}} - \sum_{\text{all } a} N_a \mu_a \quad (\text{B1})$$

where a refers to the elemental identity in the slab and N_a refers to the number of a atoms in the slab.

For SrTiO_3 specifically, we have:

$$\Omega_{\text{surf}}^{\text{SrTiO}_3} = G_{\text{slab}} - N_{\text{Sr}} \mu_{\text{Sr}} - N_{\text{Ti}} \mu_{\text{Ti}} - N_{\text{O}} \mu_{\text{O}} \quad (\text{B2})$$

The SrTiO_3 chemical potential is defined as the sum of the chemical potentials of the component elements:

$$\mu_{\text{SrTiO}_3} = \mu_{\text{Sr}} + \mu_{\text{Ti}} + 3\mu_{\text{O}}$$

At thermodynamic equilibrium, the chemical potential of the surface is equal to the bulk crystal Gibbs free energy:

$$\mu_{\text{SrTiO}_3} = g_{\text{SrTiO}_3}^{\text{bulk}}$$

Substituting, we obtain:

$$\Omega_{\text{surf}}^{\text{SrTiO}_3} = G_{\text{slab}} - N_{\text{Ti}} g_{\text{SrTiO}_3}^{\text{bulk}} - \Gamma_{\text{Sr}}^{\text{Ti}} \mu_{\text{Sr}} - \Gamma_{\text{O}}^{\text{Ti}} \mu_{\text{O}} \quad (\text{B3})$$

where $\Gamma_a^{\text{Ti}} = N_a - N_{\text{Ti}} \frac{N_a^{\text{bulk}}}{N_{\text{Ti}}^{\text{bulk}}}$ refers to the excess a component in the surface with respect to the number of Ti atoms and $\frac{N_a^{\text{bulk}}}{N_{\text{Ti}}^{\text{bulk}}}$ refers to the bulk stoichiometric ratio of a to Ti.

The bulk Gibbs free energy for a crystal can be decomposed into the following:

$$g_a^{\text{bulk}} = E_a + E_a^{\text{vib}} - Ts_a + pv_a \quad (\text{B4})$$

where E_a is the static crystal energy, E_a^{vib} is the vibrational component, s_a is the entropy, and v_a is the volume of the crystal. By performing approximations similar to [47, 48], changes in E_a^{vib} due to temperature roughly cancel out changes in Ts_a while pv_a is negligible.

Thus, Gibbs free energies can be approximated by the DFT energies:

$$g_a^{\text{bulk}} \approx E_a^{\text{bulk}}$$

For later convenience in plotting the phase diagram, bulk-subtracted chemical potentials are introduced for Sr and Ti:

$$\mu'_{\text{Sr}} = \mu_{\text{Sr}} - g_{\text{Sr}}^{\text{bulk}} \approx \mu_{\text{Sr}} - E_{\text{Sr}}^{\text{bulk}} \quad (\text{B5})$$

$$\mu'_{\text{Ti}} = \mu_{\text{Ti}} - g_{\text{Ti}}^{\text{bulk}} \approx \mu_{\text{Ti}} - E_{\text{Ti}}^{\text{bulk}} \quad (\text{B6})$$

where $E_{\text{Sr}}^{\text{bulk}}$ and $E_{\text{Ti}}^{\text{bulk}}$ are obtained from DFT calculations.

Similarly, μ'_O is defined with the reference state as an isolated oxygen molecule:

$$\mu'_\text{O} = \mu_\text{O} - \frac{1}{2}E_{\text{O}_2} \quad (\text{B7})$$

where E_{O_2} is the DFT total energy.

Additionally, μ_O can be defined as a function of experimental conditions, O_2 partial pressure (p_{O_2}) and temperature (T), with the following equation:

$$\mu_\text{O}(T, p_{\text{O}_2}) = \frac{1}{2} \left[E_{\text{O}_2} + \mu_{\text{O}_2}(T, p_0) + k_B T \ln \left(\frac{p_{\text{O}_2}}{p_0} \right) \right] \quad (\text{B8})$$

where $p_0 = 1$ bar is the reference pressure and $\mu_{\text{O}_2}(T, p_0)$ is the reference chemical potential obtained from NIST [55].

We swap out μ_a for μ'_a and transform to obtain:

$$\Omega_{\text{surf}}^{\text{SrTiO}_3} = \phi - \Gamma_{\text{Sr}}^{\text{Ti}} \mu'_{\text{Sr}} - \Gamma_{\text{O}}^{\text{Ti}} \mu'_\text{O} \quad (\text{B9})$$

where

$$\begin{aligned} \phi &= G_{\text{slab}} - N_{\text{Ti}} g_{\text{SrTiO}_3}^{\text{bulk}} - \Gamma_{\text{Sr}}^{\text{Ti}} g_{\text{Sr}}^{\text{bulk}} - \Gamma_{\text{O}}^{\text{Ti}} \frac{E_{\text{O}_2}}{2} \\ &\approx E_{\text{slab}} - N_{\text{Ti}} E_{\text{SrTiO}_3}^{\text{bulk}} - \Gamma_{\text{Sr}}^{\text{Ti}} E_{\text{Sr}}^{\text{bulk}} - \Gamma_{\text{O}}^{\text{Ti}} \frac{E_{\text{O}_2}}{2} \end{aligned}$$

and as a result, $\mu'_{\text{Sr}} < 0$, $\mu'_\text{O} < 0$ for thermodynamic stability.

Note: In our main text, we denote μ'_{Sr} and μ'_O as μ_{Sr} and μ_O respectively for simplicity.

VSSR-MC samples according to the grand potential Ω_G , which is equivalent to Ω_{surf} after approximations:

$$\begin{aligned} \Omega_{\text{G}}^{\text{SrTiO}_3} &= E_{\text{slab}} - T s_{\text{slab}} - N_{\text{Sr}} \mu_{\text{Sr}} - N_{\text{Ti}} \mu_{\text{Ti}} - N_{\text{O}} \mu_{\text{O}} \\ &= G_{\text{slab}} - p v_{\text{slab}} - N_{\text{Sr}} \mu_{\text{Sr}} - N_{\text{Ti}} \mu_{\text{Ti}} - N_{\text{O}} \mu_{\text{O}} \\ &\approx G_{\text{slab}} - N_{\text{Sr}} \mu_{\text{Sr}} - N_{\text{Ti}} \mu_{\text{Ti}} - N_{\text{O}} \mu_{\text{O}} \\ &= \Omega_{\text{surf}}^{\text{SrTiO}_3} \end{aligned} \quad (\text{B10})$$

Appendix C Additional figures

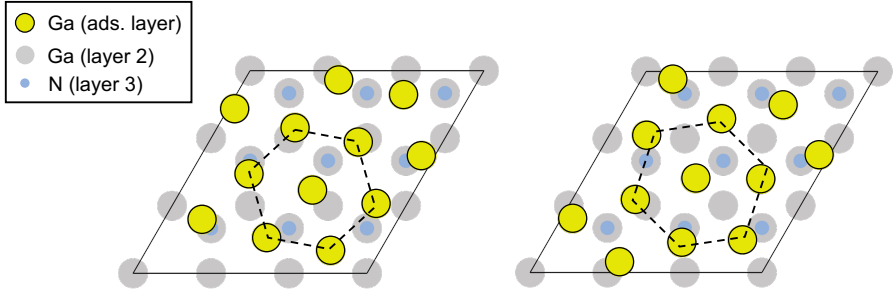


Fig. C1 Top view of additional GaN(0001) MC-sampled structures. The surface reconstruction is rotated in comparison with the reference structure from *Northrup et al.* but contains the same hexagonal patterns.

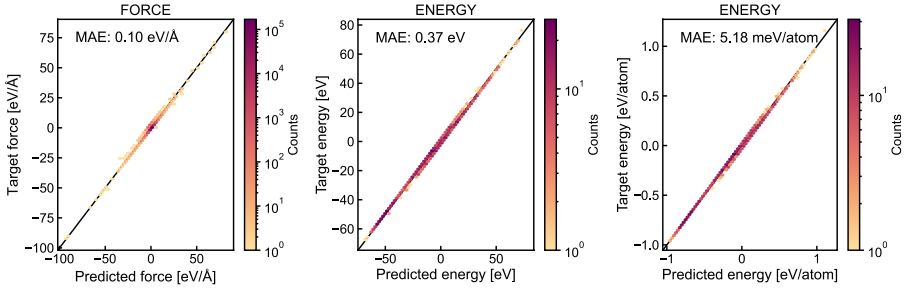


Fig. C2 Test performance of the best NFF model. As described in the main paper, the test data is obtained from VSSR-MC runs using the 6th generation NFF model.

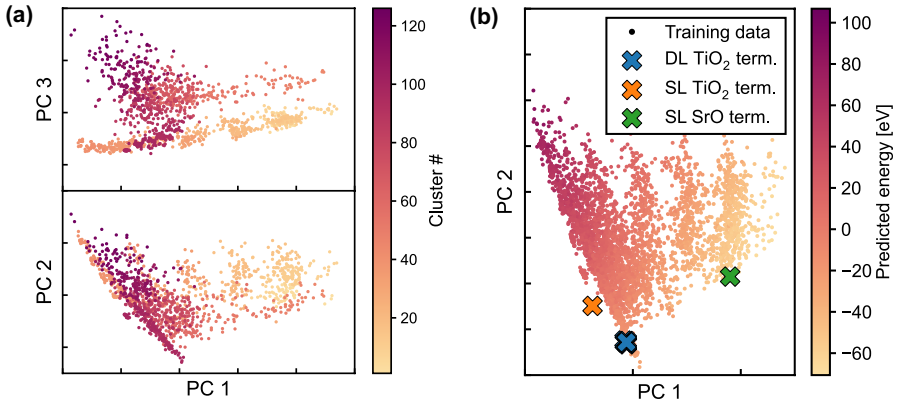


Fig. C3 Visualizations in the latent space. (a) Clustering of VSSR-MC structures in the NFF latent space visualized in the first three principal components. In the VSSR-MC with clustering AL method, the surface from each cluster with the highest force standard deviation is selected for DFT evaluation. (b) PCA of training data and the dominant terminations in the latent space of the 6th generation model.